ADVANCED INTELLIGENT SYSTEMS Open Access
www.advintellsyst.com

Electrically Controlled Liquid Crystal Elastomer Surfaces for Dynamic Wrinkling

*Zefang Li, Gina Olson, Dinesh K. Patel, Lining Yao, and Carmel Majidi**

Liquid crystal elastomers (LCEs) are becoming increasingly popular as a shape memory material for soft robot actuators that operate in a contractile or flexural mode. There have been previously studies on the use of LCEs for reversible changes in surface topography. However, surface protrusions have typically been limited to the order of 1 μm or depend on light, heat, or electrical stimulation that are difficult to locally control or require relatively high voltage. This article presents a novel operation mode of LCE actuators based on the wrinkling behavior of an LCE-elastomer bilayer architecture. Embedding a liquid-metal-based conductive ink within the LCE enables electrical control of surface wrinkling through Joule heating. The actuator cells can generate wrinkles with amplitudes ranging from 17 to 45 μm within 30 s under an input power of 2 W and a voltage on the order of 1 V. As the bilayer is composed entirely of soft materials, it is highly deformable, flexible, and can be integrated into a multi-cell array capable of bending on curved surfaces.

1. Introduction

Shape memory materials are deformable materials that recover their original shape under heat, light, or electrical stimulation.[1] Shape memory polymers (SMP) and shape memory alloys (SMA) have been utilized as artificial muscle actuators for a variety of applications in soft and bioinspired robotics.[2,3] Such actuators typically deform through contraction, bending, or torsion, as in the case of coiled SMA actuators.[4–12] Liquid crystal elastomers (LCEs) are a special class of SMP that combine the anisotropic properties of liquid crystals with the elastic properties of loosely cross-linked polymers[13] and recently have attracted interests in the field of soft robotics.[14] Typical modes of actuation of LCE are based on heat- or light-induced contraction or bending,[15–23] which are primarily used in linear or flexural actuators for soft robotics. Dynamic surface change as a novel actuation mode has been studied with different soft material systems.[24,25] As stimuli-responsive materials, LCEs can potentially lead to new opportunities for surface topography actuation in robotics, human–computer interaction, and other engineering applications.

Dynamic surface changes at small scales in LCE-based material systems have been previously studied in the context of mechanical, thermal, chemical, electrical, and light stimulation. Microscopic textured features of fine scales have been widely observed in the polydomain–monodomain transition of LCE,[26–28] which can be controlled by adding mechanical stretch and/or external heat. Nonetheless, this kind of texture change is of a very small scale (e.g., 2–3 μm, as had been previously observed in ref. [26]). Moreover, such deformations are largely in-plane with minor change in surface topography, which make the textures less distinctive and barely perceivable without microscopes. Surface change can be programmably achieved with Miura-ori actuators in response to temperature up to 150 °C and solvents such as acetone.[29] Surface protrusion was also achieved at elevated temperatures with a textile composite structure based on LCE and a plain-weave textile sheet.[30] A dynamic surface changing mechanism with LCE coatings based on high in-plane electric fields (7.5–16 V μm^{-1} and 70–80.6 V) was reported in refs. [31–33] and was shown to produce wrinkle heights on the order of hundreds of nanometers. Moreover, surface changes can also be programmed and controlled with UV light. Elastic body waves that involve deformation over the entire thickness of a thin LCE film were achieved with heating after selectively cross-linking with UV light some parts of the surface in the monodomain nematic phase.[34] Surface elevations and depressions on the order of tens and hundreds of nanometers can also be achieved by heating after preprogramming with plasmonic photoalignment.[35] UV light can be applied for controlling LCE coatings to achieve surface protrusions on the order of 1 μm.[36]

Another approach to achieving surface topography change in LCEs is through surface wrinkling of bilayer architectures with

Z. Li, C. Majidi
Department of Mechanical Engineering
Carnegie Mellon University
Pittsburgh, PA 15213, USA
E-mail: cmajidi@andrew.cmu.edu

G. Olson
The Mechanical and Industrial Engineering Department
University of Massachusetts
Amherst, MA 01003, USA

D. K. Patel, L. Yao
Human-Computer Interaction Institute
Carnegie Mellon University
Pittsburgh, PA 15213, USA

The ORCID identification number(s) for the author(s) of this article can be found under https://doi.org/10.1002/aisy.202200402.

© 2023 The Authors. Advanced Intelligent Systems published by Wiley-VCH GmbH. This is an open access article under the terms of the Creative Commons Attribution License, which permits use, distribution and reproduction in any medium, provided the original work is properly cited.

DOI: 10.1002/aisy.202200402

residual stresses or stiffness mismatches. Surface wrinkling of compliant materials achieved by bonding with stiff films such as metal film[37] or silicon film[38] has been analyzed analytically. A phase diagram of compliant film on prestretched compliant substrate was also proposed for biofilms,[39] which can be harnessed for surface instabilities, including wrinkling. Furthermore, the surface wrinkling behavior of LCE bonded with stiffer thin films has also been observed experimentally[40,41] and analyzed theoretically.[42,43]

Different potential actuation modes of surface topography change have been observed in LCE material architectures, but there is still a gap in generating surface protrusions or wrinkle heights in relatively larger scales (on the order of 10 μm) and more significant changes in surface topography electrically with lower powers (on the order of 1 V).

In this article, we present an LCE-elastomer bilayer architecture with a soft embedded Joule heating element that is capable of reversible changes in surface wrinkling through electrical stimulation. Our primary contribution is the use of an elastic bilayer and the ability to use electrical input to activate a shape memory response in LCE and convert this to surface wrinkling. To make the bilayer fully soft and elastic, we utilize a soft UV-curable elastomer that allows larger wrinkle heights on the order of 10 μm and makes the topography changes more significant. Moreover, rather than embedding serpentine copper wires as had previously been reported to enable electrical Joule heating,[18] we embed the LCE with a soft and highly stretchable conductive ink[44,45] composed of thermoplastic elastomer, silver nanoflakes, and liquid metal alloy. With Joule heating, the input voltage can stay at an order of 1 V, which is significantly lower than other electrical activation methods. As the bilayers are electrically stimulated rather than activated through external heating, we can place multiple surfaces close together in an array and independently control their surface wrinkles. This ability to individually address bilayer cells within an array has the potential to advance the use of LCE for dynamic topography change in applications ranging from a cutaneous display for human–computer interaction to a friction tuning interface for soft robot grippers.

The article is structured as follows. In Section 2, we describe the design and fabrication of the LCE-elastomer bilayer material architecture as well as a multi-cell surface wrinkling system. In Section 3, the single-cell surface wrinkling actuator design is experimentally tested in terms of bonding force, heating and contraction performance, wrinkle height and period, cycle test, and functionality of a multi-cell actuation system in curved states. We also demonstrate the functionalities of the single- and multi-cell devices and indicate their potential applications such as braille display. In Section 4, we conclude with a summary and discussion on possible future directions.

2. System Overview

2.1. Single-Cell Actuator Design

LCEs are shape memory materials that can undergo shape morphing via heat-induced nematic–isotropic phase transition. Prestretched LCE after a two-stage thiol–acrylate Michael addition and photopolymerization (TAMAP) reaction can shrink and stretch actively upon heating and cooling. As described below, we convert this shape memory response to surface wrinkling through a bilayer architecture that induces residual stresses within the LCE during actuation.

The surface wrinkling system is composed of two parts: a piece of prestretched LCE and two thin layers of UV-curable elastomer, as shown in **Figure 1**a,b. A uniaxial prestretch (λ) of 1.5 is applied to the LCE. This stretch is selected because a monodomain of bulk LCE with this stretch can usually fully recover its original shape upon heating.[46] While the surface is flat at this stretch (Figure 1c), the prestretched LCE will shrink back to its original size when heated to around 70 °C (Figure 1d). The phase transition temperature is approximately 68.3 °C, and the measurement details are in the Figure S1, Supporting Information. During heating, the LCE substrate will actively contract along its director while the elastomer coating will not, resulting in surface wrinkling.[41] The TAMAP reaction enables the LCE to stretch again when being cooled after heat-induced shrinkage. After the first-stage cross-linking with thiol-Michael addition reaction, thin layers of UV-curable elastomer are cured onto the surfaces of prestretched LCE with UV light. Under UV light, the second-stage cross-linking of LCE via free-radical reaction is also initiated by the photoinitiator.[47] The wrinkles can be removed when the LCE is cooled because the internal bonding within acrylate groups established during the second stage can drive the LCE toward its monodomain nematic phase in the prestretched state.

A single-cell of the surface wrinkling actuator is composed of a layer of LCE with an embedded serpentine conductive elastomer trace. The overall size of the cell before applying the prestretch is $24 \times 9.3 \times 2$ mm. After a $\lambda = 1.5$ prestretch of the LCE layer, residual stresses cause the dimensions of the cell to change to $16 \times 14 \times 1.3$ mm, as indicated in Figure 1c. The serpentine conductive elastomer is composed of silver flakes and microscale droplets of eutectic gallium–indium liquid metal alloy embedded in a thermoplastic elastomer and has a height of 0.2 mm, width of 0.4 mm, and pitch of 1 mm. UV-elastomer coatings with dimensions of 9×9 mm are applied to both surfaces of LCE by depositing with a stencil mask after the prestretch is applied. The nominal coating thickness is 80 μm. The embedded conductive elastomer serves as a Joule heating element that heats up the LCE and induces a shape memory response. As the prestretched LCE is heated, it undergoes a shape memory response in which it contracts to its original size prior to the prestretch, as shown in Figure 1d. The coated UV-curable elastomer, however, will not actively shrink, and this will result in internal residual stresses that cause the surface change from flat (Figure 1e) to wrinkled (Figure 1f). When electrical Joule heating is terminated, the temperature of the single-cell actuator will decrease under ambient conditions and LCE will restretch so that the wrinkles are removed (Figure 1e). Surface topographical image of a wrinkled cell reconstructed from the GelSight probe data is also shown in Figure 1f, where the amplitudes of surface wrinkles are amplified by 10 times to be better illustrated in the side view. The surface wrinkles form a clear sine wave pattern.

Figure 1g illustrates the flexibility of the single-cell actuator, where it is flexed between two fingers. This is because the entire cell is composed of soft materials.

© 2023 The Authors. Advanced Intelligent Systems published by Wiley-VCH GmbH

26404567, 0, Downloaded from https://onlinelibrary.wiley.com/doi/10.1002/aisy.202200402 by Carnegie Mellon University, Wiley Online Library on [12/04/2023]. See the Terms and Conditions (https://onlinelibrary.wiley.com/terms-and-conditions) on Wiley Online Library for rules of use; OA articles are governed by the applicable Creative Commons License

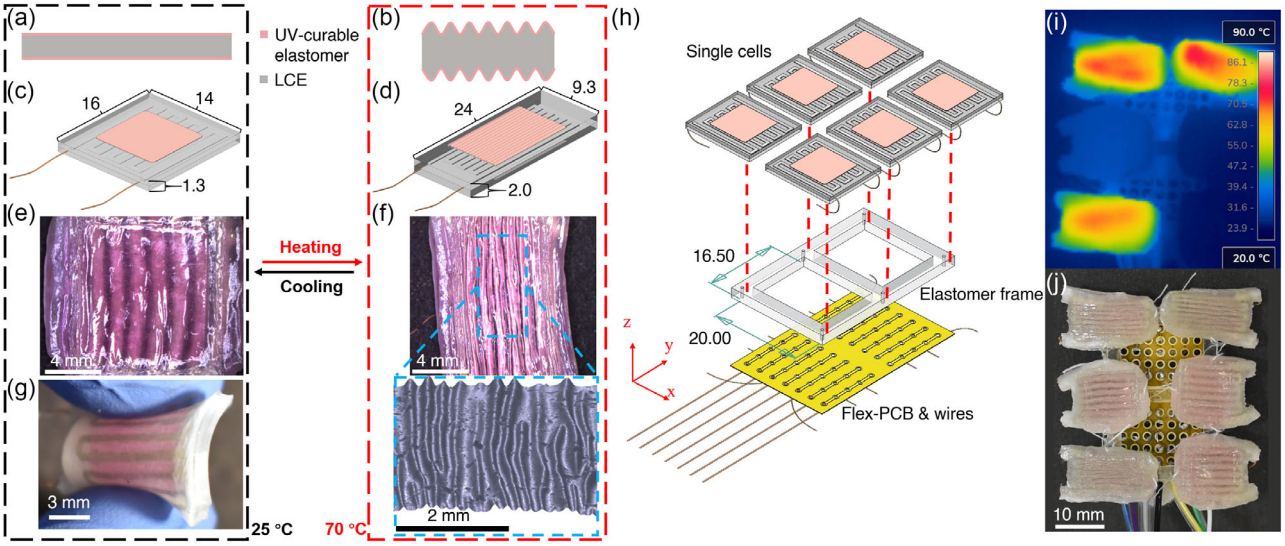

Figure 1. The designs of the single- and multi-cell surface wrinkling actuators. Sketches of the wrinkling mechanism a) at 25 °C and b) at 70 °C. LCE shrinks and generates wrinkles upon Joule heating, and removes wrinkles upon cooling. The elastomer layers are in pink and the prestretched LCE is shown in gray. c) The dimensions of the prestretched cell and d) the wrinkled cell in mm. e) Photo of a single-cell actuator before and after wrinkling. f) Photo of a single-cell actuator when generating wrinkles, by a microscope (FT-UMS1002; Femtotools), and reconstructed surface topography of a cell from measured data of GelSight probe, the wrinkle amplitude is amplified by 10 times. g) Side view of a cell being squeezed using two fingers. h) Exploded/schematic view of the assembled six-cell wrinkling surface. i) Thermal image and j) photo of the assembled six-cell wrinkling surface with wrinkles generated in three of the six cells.

2.2. Multi-Cell Array Design

The single-cell design allows for reversible transitions between smooth and wrinkled states. Because such transitions are controlled through local electrical stimulation, we can combine cells into an array in which individual cells can be independently activated. In Figure 1h, we present a six-cell array in which the individual cells are aligned in a 3×2 matrix form and connected at center to an elastomer frame, as indicated by the red dashed lines. The center-to-center distance in x and y direction is 20 and 16.5 mm, respectively. Such spacing gives some room for the extended cells when generating wrinkles, as the cells extend in the x direction and shrink in the y direction. A flex-PCB is attached to the back of the elastomer frame for connecting each cell to the microcontroller and power supply. The cells are electrically connected in parallel with six ports for power input and a common ground. Jumper wires are soldered to the flex-PCB for connection to the microcontroller and power supply. The thermal image and the photo of the assembled array with wrinkling activated in three of the six cells are shown in Figure 1i,j.

3. Results and Discussion

Here, we present the characteristics of the surface wrinkling LCE architecture. The overall thermal response of a single cell is analyzed in terms of contraction with time and temperature. The wrinkle amplitudes for different elastomer coating thickness are also measured. To understand the response of the cell to repetitive activation, we examine the electrical resistance of the Joule heating element over multiple actuation cycles. Finally, we present a flexible multi-cell surface and demonstrate the ability to independently activate individual cells without interfering with neighbor cells.

3.1. Thermal Response of a Single-Cell Actuator

The single-cell design can either generate wrinkles or remove wrinkles upon heating, and Joule heating achieved with the embedded conductive elastomer traces enables on-board heating through direct supply of electrical current. Its functionality is demonstrated as follows. Before generating the wrinkles, the single-cell device is at ambient temperature and the elastomer surface is flat and no wrinkling is present (Figure 1e). When the cell is heated by a power supply via Joule heating, LCE starts to shrink and wrinkles appear as shown in Figure 1f. The wrinkles can be removed if Joule heating is stopped and the cell is cooled to below 40 °C, and the surface turns flat and smooth again (Figure 1e).

Three single-cell actuators are tested under three different input power levels for three repeated cycles. For each test, the contraction of the cell and the average temperature on the cell surface are captured with an optical and a thermal camera simultaneously. The cell is heated up from room temperature at around 25 °C to around 70 °C through electrical Joule heating and cooled down to room temperature through ambient cooling. The input power to the embedded Joule heater is controlled by a power supply with controlled voltage.

The effect of temperature to the contraction for all the 27 tests is shown in **Figure 2**a. Even if different power levels are indicated with different colors, the overall contraction-temperature curve is still not distinguishable by different powers. This is because all the three applied power levels result in quasistatic heating, and

© 2023 The Authors. Advanced Intelligent Systems published by Wiley-VCH GmbH

26404567, 0, Downloaded from https://onlinelibrary.wiley.com/doi/10.1002/aisy.202200402 by Carnegie Mellon University, Wiley Online Library on [12/04/2023]. See the Terms and Conditions (https://onlinelibrary.wiley.com/terms-and-conditions) on Wiley Online Library for rules of use; OA articles are governed by the applicable Creative Commons License

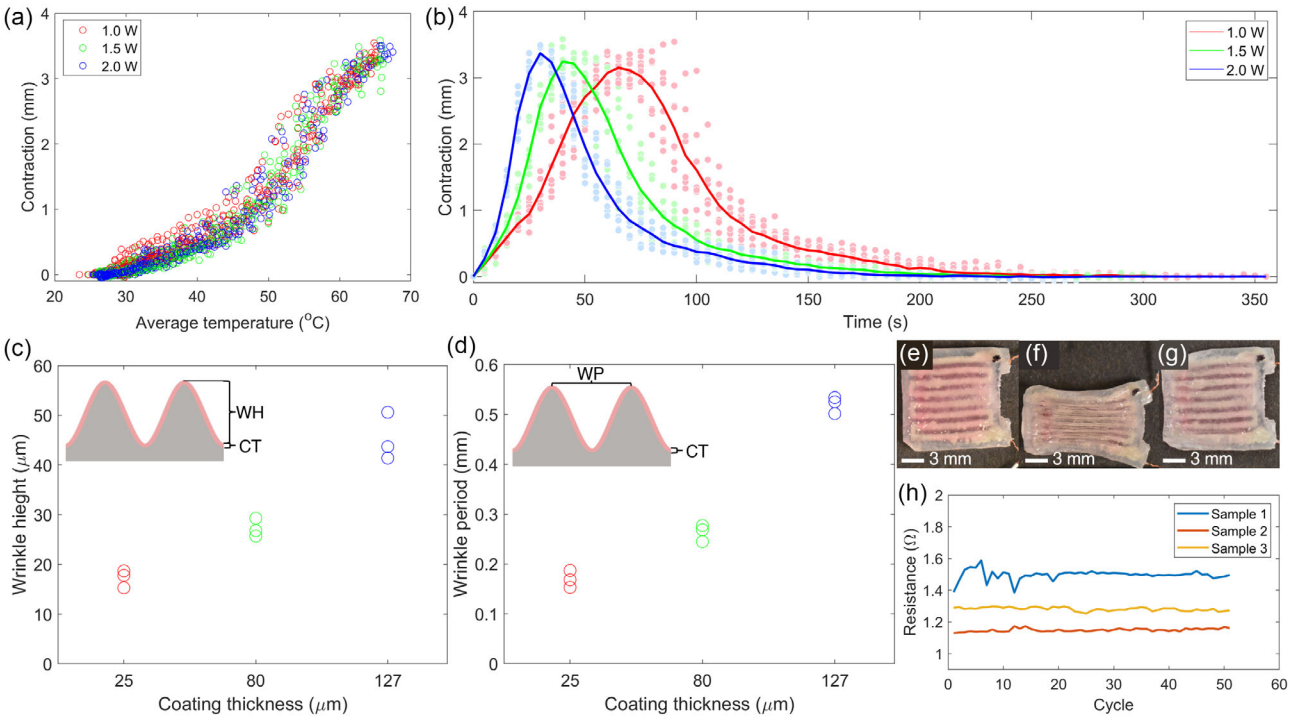

Figure 2. Single-cell surface wrinkling actuator characteristics. a) Contraction of cells at different temperatures. b) Contraction of cells versus time for cells at different input powers. c) Wrinkle heights (WH) and d) wrinkle periods (WP) for cells with different UV-curable elastomer coating thicknesses (CT). Photos of a sample cell e) before, f) during one cycle of, and g) after 50 cycles of the cyclic tests. h) Resistance of the cells after each of the 50 cycles.

consequently all the tested cells have a similar curve under different input power levels. On the other hand, different input power levels will result in different times for contraction. As the input power increases, the temperature of a single cell will increase faster, and consequently contraction also happens faster. The input powers of 1, 1.5, and 2 W results in actuation time of 65, 40, and 30 s, respectively, as shown by the three averaged curves of the three power levels in Figure 2b. As the input power increases, the actuation time decreases (Figure 2b). It takes around 200 s for the single cell to cool down and extend back to the original length, and the wrinkles are observed to be fully removed when the contraction is less than around 1 mm.

3.2. Wrinkle Characterization

Wrinkle heights for different coating thicknesses of UV-curable elastomer are characterized with a GelSight tactile sensor that can rapidly measure surface topography via contact. For each measurement of the surface topography, one profile along a line perpendicular to the wrinkles is randomly selected and extracted. Each profile contains three successive periods of wrinkles. The wrinkle height for the profile is obtained by taking the average of the differences between the peak and valley heights in each period. The wrinkle period is obtained by taking the average distances between the three peaks in the profiles. The data processing details are described in Figure S2, Supporting Information.

Figure 2c shows the results for characterization of wrinkle height. For coating thicknesses of 127, 80, and 25 μm, the wrinkle heights are measured as 45, 27, and 17 μm, respectively. These wrinkle heights are of one order or two higher than previous works on dynamic surface based on LCE. As the coating thickness increases, the wrinkle height also increases. This trend aligns with results from previous works on wrinkling behavior of polystyrene film on soft substrates.[48] The amplitude of wrinkles that can be perceptible by human finger ranges from micrometer scale down to 13 nm,[49] which indicates that the wrinkles generated by the cells with the three elastomer coating thicknesses can be perceived by human finger. This suggests that this surface wrinkling actuator may have applications in haptics and human–computer interaction. The wrinkle periods for the three coating thicknesses are shown in Figure 2d. As the coating thickness increases from 25 to 127 μm, the wrinkle period increases from 0.169 to 0.264 mm and then to 0.520 mm. These period measurements have similar trends as that reported in ref. [41] and achieve a magnitude of one order higher.

The thickness of LCE can also affect the wrinkling characteristics. When the UV-curable elastomer coating thickness remains the same, a thicker LCE substrate will yield a larger wrinkle height and wavelength (Figure S5 and S6, Supporting Information).

3.3. Cyclical Testing

The single-cell design is tested under cycles of Joule heating and ambient cooling. Three surfaces of interest on three single-cell devices can be activated for 50 cycles with no observable damage.

© 2023 The Authors. Advanced Intelligent Systems published by Wiley-VCH GmbH

26404567, 0, Downloaded from https://onlinelibrary.wiley.com/doi/10.1002/aisy.202200402 by Carnegie Mellon University, Wiley Online Library on [12/04/2023]. See the Terms and Conditions (https://onlinelibrary.wiley.com/terms-and-conditions) on Wiley Online Library for rules of use; OA articles are governed by the applicable Creative Commons License

Figure 2e shows a sample surface of one cell before the cyclical test. During one cycle, the cell is heated to 75 °C by a power supply (CSI3010SW; Circuit Specialists Inc.) that supplies an electrical power of 1.5 W. It is then cooled to around 30 °C. The cell deformation after one cycle is shown in Figure 2f. After each cycle, the resistance of the conductive elastomer is measured with a multimeter (34401A; Agilent Technologies). Figure 2h shows the resistances for the three samples after each cycle, and no significant change in resistance is observed. Figure 2g shows the sample surface after 50 cycles, and no significant difference from Figure 2e is observed.

3.4. Peel Test

Although UV-curable elastomer sheets are observed to easily adhere to LCE, delamination frequently occurs if there are insufficient amounts of acrylate groups in the LCE. This is because the bonding between UV-curable elastomer and LCE is established by the free radical reaction between the unsaturated bonds within UV-curable elastomer resin and LCE. Therefore, in order to build devices out of the UV-curable elastomer and LCE that are durable and have less chance of delamination, we need to investigate the effect of different formulations of LCE on the adhesion between the two materials.

Peel tests based on the ASTM D1876 standard with some modifications are performed on different LCE formulations where the total amount of RM257 and ratio of EDDET to PETMP are controlled. Referring to Figure S3a, Supporting Information, peel tests are performed on a Model 5969 Instron materials testing machine with a peeling speed of 127 mm min^{-1}. The molar ratios of the acrylate group to thiol group of 10:8, 10:9, 10:10, and 10:11 are used for the testing specimens. The specimen size is 76.3 × 12.5 mm, as shown in Figure S3b, Supporting Information. Referring to **Figure 3**b, peeling the sample results in a peak force followed by a "steady-state" force that is reached well before 15.9 mm of peel displacement is achieved. Therefore, we calculate the steady-state peel force as the force measured after a displacement of 15.9 mm following the peak force, as highlighted with solid lines in the raw force–displacement data. We note that the UV-curable elastomer often tears before peeling happens. LCE can also be further stretched during test which can cause inaccuracy in the steady-state peel force measurement. Therefore, in order to ensure that peeling happens at the interface between LCE and UV-curable elastomer at a controlled speed, both the UV-curable elastomer and LCE are attached to a layer of paper that provides mechanical reinforcement to prevent material failure this ensures consistency between gripper displacement and peel displacement and helps keep the peel displacement the same across the width of the specimen (Figure 3a). This structure helps make sure that the peel happens on the interface between LCE and the UV-curable elastomer, which can be validated by the clean debonding that is observed after peel (Figure S3c, Supporting Information).

A higher peel force indicates a stronger bonding between the two materials. As shown in Figure 3c, as the ratio of the acrylate group to thiol group decreases in the LCE formulation, the peel force decreases significantly. This is reasonable because a higher molar ratio of acrylate group to thiol group in the formulation indicates more available acrylate groups within the resulted LCE for bonding with the UV-curable elastomer. Therefore, in order to achieve better bonding between UV-curable elastomer and LCE, a higher molar ratio of acrylate group to thiol group in the LCE formulation is desired. Nevertheless, as the amount of thiol group decreases relative to the amount of acrylate groups, LCE becomes less densely cross-linked and less stiff, which makes it harder to generate surface wrinkles. Considering both factors, a molar ratio of 10:9 is adopted for the acrylate and thiol groups. The detailed LCE composition selection procedure is described in the Figure S4, Supporting Information.

3.5. Multi-Cell Array

A six-cell array of the wrinkling LCE cells is used to demonstrate the ability to activate individual cells through localized electrical Joule heating. **Figure 4**a presents the Braille-like array with cells arranged in a 3 × 2 array. In its natural state at room temperature, the cells are fully stretched and smooth, with no surface wrinkles. As shown in Figure 4b through d, three cells are individually activated to produce the surface wrinkle patterns

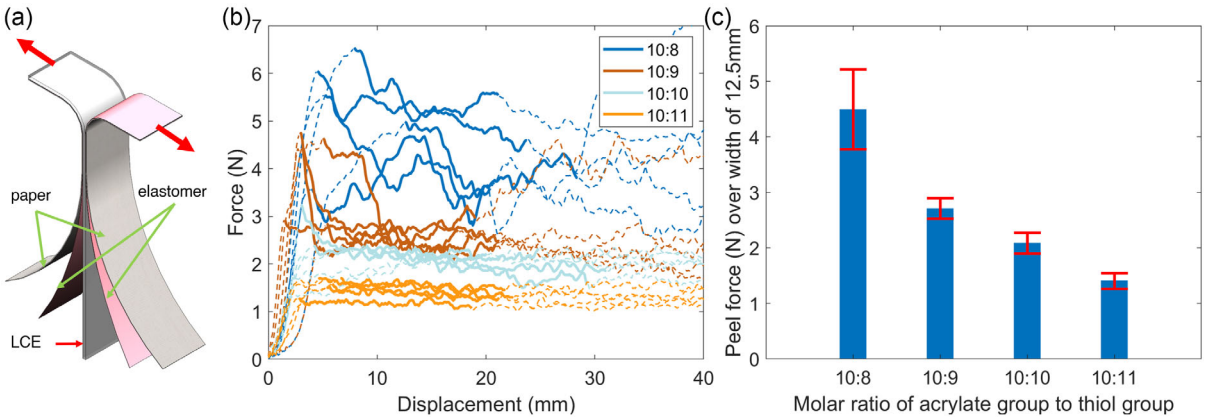

Figure 3. Peel test specimen, and results. a) Peel test specimen structure. The red arrows indicate the direction of peel force. b) Force–distance raw data from the peel test, solid lines indicate the part of data used to calculate average force. c) Peel test results.

© 2023 The Authors. Advanced Intelligent Systems published by Wiley-VCH GmbH

26404567, 0, Downloaded from https://onlinelibrary.wiley.com/doi/10.1002/aisy.202200402 by Carnegie Mellon University, Wiley Online Library on [12/04/2023]. See the Terms and Conditions (https://onlinelibrary.wiley.com/terms-and-conditions) on Wiley Online Library for rules of use; OA articles are governed by the applicable Creative Commons License

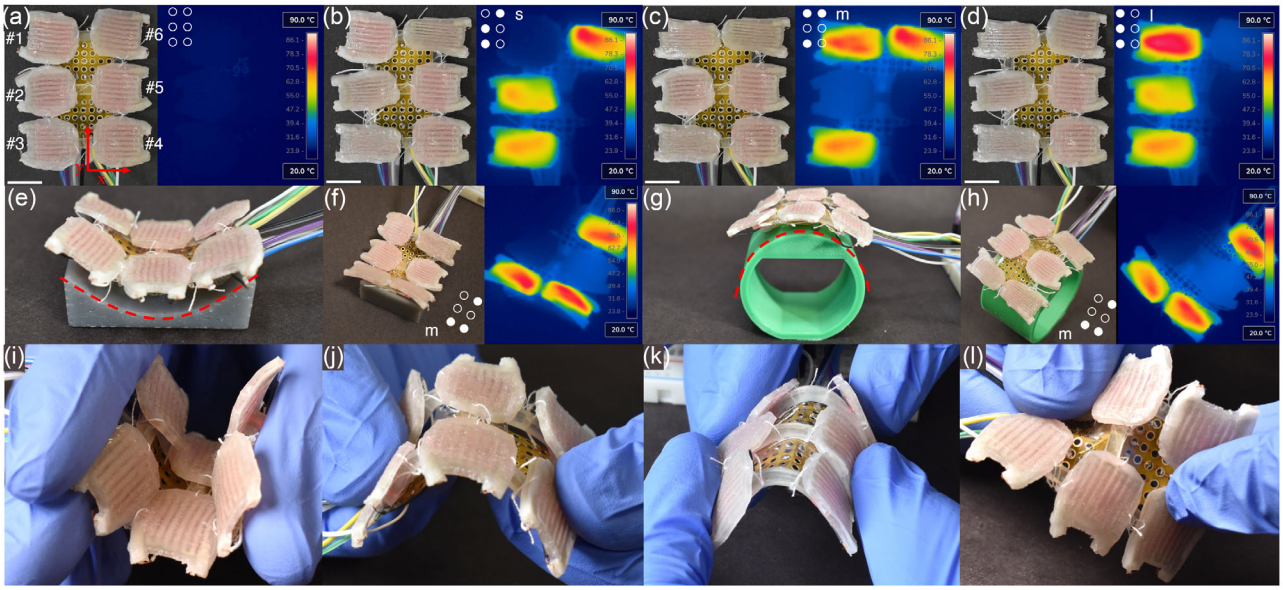

Figure 4. Multi-cell device generating different wrinkled surfaces on a flat, concave, and convex surfaces. The braille-like device has 3 rows (each along *x* direction) and 2 columns (each along *y* direction). a) The six-cell device on a flat surface with no wrinkle generated. b) One cell in the each row #2, #3, #6 is activated; this resembles lower case English braille letter "s". c) Cells #2, #3, #6 are activated, replicating English braille "m". d) Cells #1, #2, #3 in the same column are activated, replicating English braille "l". e) Side view of the six-cell device on a concave fixture with radius of 22.28 mm. f) The six-cell device generating a pattern of surface wrinkles corresponding to braille "m" in the concave fixture. g) Side view of the six-cell device on a convex fixture with radius of 22.28 mm. h) The six-cell device generating a pattern of surface wrinkles corresponding to braille "m" in the convex fixture. The six-cell device bent in hand i) concavely, j) convexly, and k) convexly along another direction. l) The six-cell device twisted in hand.

corresponding to Braille characters for "s", "m", and "l" (standing for the "Soft Machines Lab"). The ability to create these Braille-like characters is possible through localized Joule heating using the embedded conductive ink. In this way, each cell does not mechanically or thermally affect the actuation of any other cell, and can be activated or deactivated independently. In contrast, it would be relatively challenging to activate individual cells using an external source such as a heat gun or a lamp.

Because it is mostly composed of intrinsically soft materials, a multi-cell array can conform to surfaces of different curvatures while maintaining its functionalities. To demonstrate this property, the array is placed on concave (Figure 4e) and convex (Figure 4g) fixtures. The radii of both convex and concave curvatures are 22.28 mm. Figure 4f,h show the six-cell array with actuated surface wrinkles corresponding to English braille "m" on the two curvatures. The cells can still be independently actuated without interfering with the state of the adjacent cells. Additionally, the array can also be bent (Figure 4i–k) and twisted without mechanical failures.

4. Conclusion and Future Work

Here, we present an LCE-elastomer bilayer architecture capable of reversible surface wrinkling through electrical stimulation. The design and fabrication of single- and multi-cell devices are reported. The thermal response, wrinkle characterization, and cyclic testing, and bonding force between LCE and UV-curable elastomer of the single-cell actuator are analyzed and presented, which provides a guidance on designing of texturing changing actuators using the LCE wrinkling mechanism. The multi-cell device is demonstrated when bending at different curvatures, where the functionality of each cell does not affect one another.

Surface wrinkling actuators made of LCE-elastomer bilayers have many potential applications. For instance, wrinkled and patterned surfaces have been shown to enhance adhesion.[50–53] Surface textures based on wrinkles are also shown to enable adaptive camouflage,[54,55] which is also a potential application for an LCE-based surface wrinkling actuator. Moreover, some of the surface wrinkles this actuator generates can be felt by human skin and hence the actuator can be used for haptic interfaces such as cutaneous displays.

Another future direction of this work is the theoretical analysis of the wrinkling behavior of LCE bonded with general elastomers. Previous analysis done by Goriely and Mihai[42] will become less accurate for films that are not significantly stiffer than the LCE substrate, which is our case, and a nonlinear analysis of this instability needs to be studied. Additionally, the experimental analysis of the surface wrinkling with respect to different film–substrate thickness ratios with improved noncontact surface profilometry is another future direction.

5. Experimental Section

Single-Cell Fabrication: The first step of fabrication is to print the serpentine conductive elastomer trace on the bottom of a mold of 1 mm thick through direct ink writing (DIW). Conductive inks based on eutectic gallium–indium (EGaIn) have been widely studied.[44,56,57] Here, we adopt a conductive elastomer that is prepared with a procedure

 © 2023 The Authors. Advanced Intelligent Systems published by Wiley-VCH GmbH

26404567, 0, Downloaded from https://onlinelibrary.wiley.com/doi/10.1002/aisy.202200402 by Carnegie Mellon University, Wiley Online Library on [12/04/2023]. See the Terms and Conditions (https://onlinelibrary.wiley.com/terms-and-conditions) on Wiley Online Library for rules of use; OA articles are governed by the applicable Creative Commons License

adapted from Zu et al.[45] First, the liquid metal EGaIn of 3.0 g and silver flakes (SF91; Ames-Goldsmith) of 1.24 g are added to a 20 mL glass vial. Then, a 1.000 g solution of polystyrene-block-polyisoprene-block-polystyrene (SIS) copolymer elastomer is added. The SIS solution is prepared by dissolving SIS pellets (14 wt% of styrene; Sigma–Aldrich) into toluene (Sigma–Aldrich) (15 wt% SIS) at 100 °C for 48 h. The SIS solution, EGaIn, and silver flakes are then mixed by a planetary centrifugal mixer (AR-100; Thinky Corporation) for 3 min at 2000 RPM, and transferred to a 10 mL syringe with 27 G Luer tip. With an extrusion-based DIW 3D printer (30 m; Hyrel 3D), the conductive ink can be used to print the serpentine trace in the 25 × 25 × 1 mm mold (Figure S7a, Supporting Information). Conductive wires of 36 gauge are then connected to the traces using the conductive ink, after which the conductive elastomer traces are ready to add LCE layers.

The LCE fabrication procedure is adapted from Yuan et al.[58] RM257 monomer (1,4-bis-[4-(3-acryloyloxypropyloxy)benzoyloxy]-2-methylbenzene) (5.000 g; ChemScence LLC; 96.55%) is first dissolved into 1.550 g toluene (Sigma–Aldrich) at 80 °C for 20 min. After cooling the solution down to room temperature (25 °C), 0.0130 g photoinitiator HHMP ((2-hydroxyethoxy)-2-methylpropiophenone) is added to the above solution, and the solution is heated at 80 °C for 20 min or until HHMP is fully dissolved. After being cooled down to room temperature (25 °C) again, 0.856 g of EDDET spacer (2,2'-(ethylenedioxy) diethanethiol; Sigma–Aldrich), 0.720 g of PETMP crosslinker (pentaerythritol tetrakis (3-mercaptopropionate); Sigma–Aldrich), and 0.150 g DPA (dipropylamine; Sigma–Aldrich) solution (weight ratio of DPA to toluene of 1:15) are added to the above solution in the order as mentioned. The mixture is then mixed by the planetary centrifugal mixer (AR-100; Thinky Corporation) for 1 min at 2000 RPM, degassed for 1 min, and poured into molds with printed conductive elastomer traces (Figure S7b, Supporting Information).

Around 2 h after pouring LCE into the mold, the LCE should have cured to a large extent and become the form of less sticky elastomer. At this stage, most of the toluene solvent still remains in the LCE and the first layer of LCE has not deswelled and shrinked. The first layer is then demolded and flipped over so that the conductive elastomer trace faces upward and the first LCE layer lies at the bottom of a second mold with size of 25 × 25 × 2 mm, as shown in Figure S7c, Supporting Information. The second layer of LCE is then synthesized with the same procedure as the first layer, and poured into the second mold (Figure S7d, Supporting Information).

After 12 h, when the two layers of LCE are fully cure and bonded with each other, the LCE with embedded conductive elastomer is demolded (Figure S7e, Supporting Information) and put in a vacuum oven (AT09; Across International) at 80 °C and 508 mm of Hg for 24 h to remove the toluene solvent. Once the toluene is removed, the LCE with embedded conductive elastomer turns opaquely white and soft. It is further stretched to $\lambda = 1.5$ and cut to a size of 14.3 × 14 mm (Figure S7f, Supporting Information). Then, two layers of UV-curable elastomer are deposited on both sides of the LCE layer using a stancil mask to control the nominal thickness. To add the UV-curable elastomer, the first step is to place a stencil of 9 × 9 mm on one surface of the LCE layer. Then, the UV-curable elastomer resin is added to the stencil and deposited using with a blade (Figure S7g, Supporting Information). The stencil mask is then removed and 395 nm UV light is applied immediately after that for 35 s with a UV torch (R838; Warsun), as shown in Figure S7h, Supporting Information. Repeating this procedure on the other surface of LCE yields a fabricated single-cell surface wrinkling actuator (Figure S7i–j, Supporting Information). During this procedure, the photoinitiator HHMP within LCE will also initiate the second-stage cross-linking among the unreacted acrylate groups, which enables the single-cell devices to stretch from the wrinkled state back to flat when being cooled.

The UV-curable elastomer resin is prepared according to Patel et al.[59] The elastomeric resin is comprised of 49.015 wt% of epoxy aliphatic acrylate (EAA, Ebecryl 113; Allnex), 49.015 wt% of aliphatic urethane diacrylate (AUD; Ebecryl 8413; Allnex), 1.96 wt% TPO (diphenyl(2,4,6-trimethylbenzoyl)phosphine oxide; Genocure TPO; RAHN USA Corp.) as the photoinitiator, and 0.01 wt% pigment Rhodamine B (Sigma–Aldrich). TPO and Rhodamine B were dissolved in elastomeric monomers on a hot water bath at 86 °C.

Multi-cell Assembly: The procedure to build a multi-cell array is as follows. The first step is to build a soft frame with the UV-curable elastomer by casting it in a mold and applying UV light in a UV crosslinker (CL-1000 Ultraviolet Crosslinker; UVP) for 30 min. The elastomeric resin is comprised of 49.02 wt% of epoxy aliphatic acrylate (EAA, Ebecryl 113; Allnex), 49.02 wt% of aliphatic urethane diacrylate (AUD; Ebecryl 8413; Allnex), and 1.96 wt% TPO (diphenyl(2,4,6-trimethylbenzoyl)phosphine oxide; Genocure TPO; RAHN USA Corp.) as the photoinitiator.[12,59] TPO was dissolved in elastomeric monomers on a hot water bath at 86 °C.

After preparing the soft elastomer frame, the centers of the six cells are then connected to the soft frame with the UV-curable elastomer resin. The connections are highlighted with red dashed lines in Figure 1h. Sewing threads (60 100; Singer) are also applied to loosely connect the edges of the cells to the soft frame to protect the cells from disconnecting while allowing some movement, as shown in Figure 1j. In most cases, the sewing threads are not necessary.

Finally, the wires that connect to each cell are then soldered to a flex-PCB bread board (1518, Adafruit) along with jumpers.

Wrinkle Height Characterization: To characterize the wrinkle heights, coating thicknesses of 25, 80, and 127 μm are adopted by varying the thickness of stencils, and three single-cell samples are prepared for each thickness. For each measurement, the single-cell device is brushed with thermal grease (HY400; Halnziye), heated up to around 80 °C, and placed on a PTC Heating Element (Bestol) at around 70 °C. After placing the cell on the heat pad for 1 min, the tactile sensor (GelSight Mobile Series 1 probe; GelSight, Inc.) is placed on the top of the cell. The contacting force is controlled and provided only by the gravitational force of the tactile sensor because a larger contacting force can further deform the wrinkles affect the measurement results. After each measurement, the tactile sensor is detached immediately.

Peel Test Specimen Preparation: The procedure of preparing test specimens is as follows. After cutting towel paper (26 601; Georgia-Pacific Consumer Products LP.) into size of 76.3 × 12.5 mm, UV-curable elastomer resin is applied to the paper and brushed for 5 min or until the resin infiltrates the paper. Then, the paper with resin is cured at 395 nm UV light with a UV torch (R838; Warsun) for 30 s, and additional layer of UV-curable elastomer is brushed over the cured elastomer-paper layer. LCE of size of 25 × 50 × 1 mm is stretched along the 50 mm edge to a stretch of approximately 1.5. Then, a piece of paper with elastomer resin is added to this LCE and cured at 395 nm UV light with a UV torch (R838; Warsun) for 10 s. A second layer of paper with UV-curable elastomer resin is then added to the second surface of LCE in the same way. After that, both surfaces of the specimen are cured in a UV crosslinker (CL-1000 Ultraviolet Crosslinker; UVP) for 3 min, respectively. The overall structure of the specimen has five layers: two outermost layers of paper, two layers of UV-curable elastomer, and one layer of LCE in the middle, as shown in Figure S3b, Supporting Information.

Supporting Information

Supporting Information is available from the Wiley Online Library or from the author.

Acknowledgements

This material is based upon work supported by the U.S. Army Research Office under (Contract/grant no. W911NF1810150) and the National Science Foundation Career (grant no. IIS2047912). The authors would like to thank Dr. Wenzhen Yuan and Arpit Agarwal for providing the GelSight probe. The authors would like to thank Dr. Sarah Bergbreiter and Sukjun Kim for providing the Femtotools microscope. The authors would also like to thank Rahn USA Corporation for providing Genocure TPO and Allnex, USA for providing Ebecryl 113 (EAA) and Ebecryl 8413 (AUD) samples.

© 2023 The Authors. Advanced Intelligent Systems published by Wiley-VCH GmbH

26404567, 0, Downloaded from https://onlinelibrary.wiley.com/doi/10.1002/aisy.202200402 by Carnegie Mellon University, Wiley Online Library on [12/04/2023]. See the Terms and Conditions (https://onlinelibrary.wiley.com/terms-and-conditions) on Wiley Online Library for rules of use; OA articles are governed by the applicable Creative Commons License

Conflict of Interest

The authors declare no conflict of interest.

Data Availability Statement

The data that support the findings of this study are available from the corresponding author upon reasonable request.

Keywords

bilayer systems, liquid crystal elastomers, wrinkling

Received: November 25, 2022
Revised: February 10, 2023
Published online:

[1] W. Huang, Z. Ding, C. Wang, J. Wei, Y. Zhao, H. Purnawali, *Mater. Today* **2010**, *13*, 54.
[2] G. Scalet, *Actuators* **2020**, *9*, 10.
[3] H. Rodrigue, W. Wang, M.-W. Han, T. J. Kim, S.-H. Ahn, *Soft Rob.* **2017**, *4*, 3.
[4] B. Jin, H. Song, R. Jiang, J. Song, Q. Zhao, T. Xie, *Sci. Adv.* **2018**, *4*, aao3865.
[5] Y. Chen, X. Zhao, Y. Li, Z.-Y. Jin, Y. Yang, M.-B. Yang, B. Yin, *J. Mater. Chem. C* **2021**, *9*, 5515.
[6] M. N. I. Shiblee, K. Ahmed, M. Kawakami, H. Furukawa, *Adv. Mater. Technol.* **2019**, *4*, 1900071.
[7] Z. Hu, Y. Li, T. Zhao, J.-a. Lv, *Appl. Mater. Today* **2022**, *27*, 101449.
[8] X. Huang, K. Kumar, M. K. Jawed, A. M. Nasab, Z. Ye, W. Shan, C. Majidi, *Sci. Rob.* **2018**, *3*, aau7557.
[9] T. Hino, T. Maeno, in *Proc. of The Int. Symp. on Robotics and Automation*, Querétaro, México August **2004**, pp. 214–218.
[10] W. Wang, S.-H. Ahn, *Soft Rob.* **2017**, *4*, 379.
[11] D. K. Patel, X. Huang, Y. Luo, M. Mungekar, M. K. Jawed, L. Yao, C. Majidi, *Adv. Mater. Technol.* **2023**, *8*, 2201259.
[12] Z. J. Patterson, D. K. Patel, S. Bergbreiter, L. Yao, C. Majidi, *Soft Rob.*, *4*, 379 **2022**.
[13] S. W. Ula, N. A. Traugutt, R. H. Volpe, R. R. Patel, K. Yu, C. M. Yakacki, *Liq. Cryst. Rev.* **2018**, *6*, 78.
[14] X. Huang, M. Ford, Z. J. Patterson, M. Zarepoor, C. Pan, C. Majidi, *J. Mater. Chem. B* **2020**, *8*, 4539.
[15] D. Tang, L. Zhang, X. Zhang, L. Xu, K. Li, A. Zhang, *ACS Appl. Mater. Interfaces* **2021**, *14*, 1929.
[16] L. Chen, H. K. Bisoyi, Y. Huang, S. Huang, M. Wang, H. Yang, Q. Li, *Angew. Chem. Int. Ed.* **2021**, *60*, 16394.
[17] J. Liu, Y. Gao, H. Wang, R. Poling-Skutvik, C. O. Osuji, S. Yang, *Adv. Intell. Syst.* **2020**, *2*, 1900163.
[18] Q. He, Z. Wang, Y. Wang, A. Minori, M. T. Tolley, S. Cai, *Sci. Adv.* **2019**, *5*, aax5746.
[19] Y. Zhang, Z. Wang, Y. Yang, Q. Chen, X. Qian, Y. Wu, H. Liang, Y. Xu, Y. Wei, Y. Ji, *Sci. Adv.* **2020**, *6*, aay8606.
[20] M. Zadan, D. K. Patel, A. P. Sabelhaus, J. Liao, A. Wertz, L. Yao, C. Majidi, *Adv. Mater.* **2022**, *34*, 2200857.
[21] M. Zadan, D. K. Patel, M. H. Malakooti, L. Yao, C. Majidi, in *Smart Materials, Adaptive Structures and Intelligent Systems*, Vol. *86274*, American Society of Mechanical Engineers, New York, NY **2022**, p. V001T01A011.
[22] S. Huang, Y. Shen, H. K. Bisoyi, Y. Tao, Z. Liu, M. Wang, H. Yang, Q. Li, *J. Am. Chem. Soc.* **2021**, *143*, 12543.
[23] S. Huang, Y. Huang, Q. Li, *Small Struct.* **2021**, *2*, 2100038.
[24] W. Feng, D. Liu, D. J. Broer, *Small Struct.* **2021**, *2*, 2000107.
[25] F. L. Visschers, H. Gojzewski, G. J. Vancso, D. J. Broer, D. Liu, *Adv. Mater. Interfaces* **2019**, *6*, 1901292.
[26] S. Clarke, E. Terentjev, I. Kundler, H. Finkelmann, *Macromolecules* **1998**, *31*, 4862.
[27] J. Biggins, *Liq. Cryst.* **2009**, *36*, 1139.
[28] H. Higaki, K. Urayama, T. Takigawa, *Macromol. Chem. Phys.* **2012**, *213*, 1907.
[29] T. H. Ware, M. E. McConney, J. J. Wie, V. P. Tondiglia, T. J. White, *Science* **2015**, *347*, 982.
[30] T. Ohzono, M. O. Saed, Y. Yue, Y. Norikane, E. M. Terentjev, *Adv. Mater. Interfaces* **2020**, *7*, 1901996.
[31] D. Liu, N. B. Tito, D. J. Broer, *Nat. Commun.* **2017**, *8*, 1526.
[32] W. Feng, D. J. Broer, D. Liu, *Adv. Mater.* **2018**, *30*, 1704970.
[33] H. M. van Der Kooij, D. J. Broer, D. Liu, J. Sprakel, *ACS Appl. Mater. Interfaces* **2020**, *12*, 19927.
[34] R. Yang, Y. Zhao, *Angew. Chem.* **2017**, *129*, 14390.
[35] G. Babakhanova, T. Turiv, Y. Guo, M. Hendrikx, Q.-H. Wei, A. P. Schenning, D. J. Broer, O. D. Lavrentovich, *Nat. Commun.* **2018**, *9*, 456.
[36] D. Liu, D. J. Broer, *Soft Matter* **2014**, *10*, 7952.
[37] Z. Huang, W. Hong, Z. Suo, *J. Mech. Phys. Solids* **2005**, *53*, 2101.
[38] J. Song, H. Jiang, Z. Liu, D. Khang, Y. Huang, J. Rogers, C. Lu, C. Koh, *Int. J. Solids Struct.* **2008**, *45*, 3107.
[39] Q. Wang, X. Zhao, *Sci. Rep.* **2015**, *5*, 8887.
[40] A. Agrawal, T. Yun, S. L. Pesek, W. G. Chapman, R. Verduzco, *Soft Matter* **2014**, *10*, 1411.
[41] A. Agrawal, P. Luchette, P. Palffy-Muhoray, S. L. Biswal, W. G. Chapman, R. Verduzco, *Soft Matter* **2012**, *8*, 7138.
[42] A. Goriely, L. A. Mihai, *Nonlinearity* **2021**, *34*, 5599.
[43] H. Soni, R. A. Pelcovits, T. R. Powers, *Phys. Rev. E* **2016**, *94*, 012701.
[44] P. A. Lopes, D. F. Fernandes, A. F. Silva, D. G. Marques, A. T. de Almeida, C. Majidi, M. Tavakoli, *ACS Appl. Mater. Interfaces* **2021**, *13*, 14552.
[45] W. Zu, Y. Ohm, M. R. Carneiro, M. Vinciguerra, M. Tavakoli, C. Majidi, *Adv. Mater. Technol.* **2022**, *7*, 2200534.
[46] J. E. Marshall, S. Gallagher, E. M. Terentjev, S. K. Smoukov, *J. Am. Chem. Soc.* **2014**, *136*, 474.
[47] C. Yakacki, M. Saed, D. Nair, T. Gong, S. Reed, C. Bowman, *RSC Adv.* **2015**, *5*, 18997.
[48] R. Huang, C. M. Stafford, B. D. Vogt, *J. Aerosp. Eng.* **2007**, *20*, 38.
[49] L. Skedung, M. Arvidsson, J. Y. Chung, C. M. Stafford, B. Berglund, M. W. Rutland, *Sci. Rep.* **2013**, *3*, 2617.
[50] E. P. Chan, E. J. Smith, R. C. Hayward, A. J. Crosby, *Adv. Mater.* **2008**, *20*, 711.
[51] Y. Rahmawan, C.-M. Chen, S. Yang, *Soft Matter* **2014**, *10*, 5028.
[52] C. S. Davis, D. Martina, C. Creton, A. Lindner, A. J. Crosby, *Langmuir* **2012**, *28*, 14899.
[53] S. A. Pendergraph, M. D. Bartlett, K. R. Carter, A. J. Crosby, *ACS Appl. Mater. Interfaces* **2014**, *6*, 6845.
[54] T. Ma, J. Bai, T. Li, S. Chen, X. Ma, J. Yin, X. Jiang, *Proc. Natl. Acad. Sci.* **2021**, *118*, e2114345118.
[55] E. Kelman, R. Baddeley, A. Shohet, D. Osorio, *Proc. R. Soc. B Biol. Sci.* **2007**, *274*, 1369.
[56] H. Liu, Y. Xin, H. K. Bisoyi, Y. Peng, J. Zhang, Q. Li, *Adv. Mater.* **2021**, *33*, 2104634.
[57] P. Lv, X. Yang, H. K. Bisoyi, H. Zeng, X. Zhang, Y. Chen, P. Xue, S. Shi, A. Priimagi, L. Wang, W. Feng, Q. Li, *Mater. Horiz.* **2021**, *8*, 2475.
[58] C. Yuan, D. J. Roach, C. K. Dunn, Q. Mu, X. Kuang, C. M. Yakacki, T. Wang, K. Yu, H. J. Qi, *Soft Matter* **2017**, *13*, 5558.
[59] D. K. Patel, A. H. Sakhaei, M. Layani, B. Zhang, Q. Ge, S. Magdassi, *Adv. Mater.* **2017**, *29*, 1606000.

© 2023 The Authors. Advanced Intelligent Systems published by Wiley-VCH GmbH

26404567, 0, Downloaded from https://onlinelibrary.wiley.com/doi/10.1002/aisy.202200402 by Carnegie Mellon University, Wiley Online Library on [12/04/2023]. See the Terms and Conditions (https://onlinelibrary.wiley.com/terms-and-conditions) on Wiley Online Library for rules of use; OA articles are governed by the applicable Creative Commons License